Materials & Design 225 (2023) 111575

Contents lists available at ScienceDirect

Materials & Design

journal homepage: www.elsevier.com/locate/matdes

Rapid amorphization of CrMnFeCoNi high-entropy alloy under ultrasonic vibrations

Caitao Fan [a], Luyao Li [a], Wenxin Wen [a], Hongzhen Li [b], Jianan Fu [a], Wenqing Ruan [a], Shuai Ren [a], Sajad Sohrabi [a], Zhenxuan Zhang [a], Xiong Liang [a,*], Jiang Ma [a,*]

[a] Guangdong Key Laboratory of Electromagnetic Control and Intelligent Robots, College of Mechatronics and Control Engineering, Shenzhen University, Shenzhen 518060, China
[b] National Engineering Research Center of Near-net-shape Forming for Metallic Materials, South China University of Technology, Guangzhou, 510640, China

HIGHLIGHTS

- A facile and rapid method of solid-state amorphization is proposed.
- Ultrasonic vibration treatment enables easy crystal-amorphous transformation of high entropy alloys.
- Grain refinement is the key to the crystal-amorphous transformation, and grain boundary amorphization is the main mechanism.
- The mechanical properties of the treated samples have significantly improved.

GRAPHICAL ABSTRACT

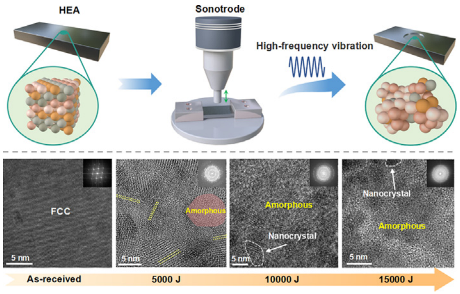

ARTICLE INFO

Article history:
Received 15 October 2022
Revised 29 December 2022
Accepted 30 December 2022
Available online 31 December 2022

Keywords:
High-entropy alloys
Amorphous phase
Ultrasonic vibration
Grain refinement

ABSTRACT

Due to the distinct design concept, high-entropy alloys (HEAs) exhibit unusual properties and lead an emerging new field. In this work, we show that a typical face-centered cubic crystalline phase CoCrFeNiMn HEA can be readily transformed into the amorphous phase under the ultrasonic vibration treatment (UVT) at a frequency of 20000 Hz. The nanoscale hierarchical features include twins, stacking faults bands, hexagonal-close packed phase bands and even amorphous bands can be obviously identified in samples treated by different UVT energies. The dominant mechanism of ultrasonic vibration-induced amorphization is that the grain refinement promotes the formation of amorphous phases when the defect density at the grain boundaries reaches a critical level. In addition, the mechanical instability is easily induced by ultrasonic vibration at high strain rate to generate amorphous phase inside the grains. As a consequence of UVT, the HEA samples revealed significant mechanical performance improvement owing to the microstructure evolution especially the generation of amorphous phase, such as yielding strength and hardness. This rapid amorphization process provides not only a candidate strengthening mechanism for HEA, but also a novel approach to unveil the pending crystal-amorphous transition problem.

© 2022 The Author(s). Published by Elsevier Ltd. This is an open access article under the CC BY-NC-ND license (http://creativecommons.org/licenses/by-nc-nd/4.0/).

1. Introduction

High-entropy alloys (HEAs) contain five or more major elements with equal or nearly equal atomic percentages, with the concentration of each element varying between 5 and 35 % [1–4]. This solid solution HEAs in a stable equiatomic multi-element alloy possesses various excellent properties such as fatigue properties, phase stability and radiation damage tolerance [5–8]. Therefore, HEAs have attracted significant attention in the last decade as a material with potentially interesting properties [9–11].

The introduction of amorphous phases to HEAs can provide additional strengthening and toughening mechanisms for its excellent properties [12–15]. The appearance of partially amorphous

---

* Corresponding authors.
E-mail addresses: xliang@szu.edu.cn (X. Liang), majiang@szu.edu.cn (J. Ma).

https://doi.org/10.1016/j.matdes.2022.111575
0264-1275/© 2022 The Author(s). Published by Elsevier Ltd.
This is an open access article under the CC BY-NC-ND license (http://creativecommons.org/licenses/by-nc-nd/4.0/).

phases in the deformation zone of HEAs under the action of extreme forces has been reported previously, such as forced shearing [13], low temperature stretching [14], high pressure torsion [15], and ball milling [16,17]. In addition, magnetron sputtering and laser melting and sinking also tend to make crystalline solid solutions amorphous owing to the rapid cooling process [18–21]. Above all, these methods that enable the conversion of ordered state crystals to disordered non-crystals are an interesting and worthwhile phenomenon to investigate, in terms of performance and mechanistical principle.

For the study of amorphization phenomenon, a novel and efficient high-frequency low-stress ultrasonic vibration treatment (UVT) is applied in this work. It is a simple, economical and flexible auxiliary method [22–25] that can improve the plasticity, strength, hardness and formability of samples in an extremely short time [26–29]. By applying UVT to the face-centered cubic (FCC) CoCrFeNiMn HEA, we were surprised to find large amorphous regions on the HEA specimens by transmission electron microscopy (TEM). Besides, a large number of dislocations, twins, stacking fault (SF), as well as hexagonal close-packed (HCP) were observed by using high-resolution transmission electron microscopy (HRTEM). In terms of mechanical properties, the CoCrFeNiMn HEA treated with UVT showed a significant increase in hardness and yield strength. Our results show that UVT could be a novel strategy that transforms metal materials such as HEAs from crystalline to amorphous state.

2. Materials and methods

2.1. Materials preparation

Nominal composition $Co_{20}Cr_{20}Fe_{20}Ni_{20}Mn_{20}$ (at.%) HEA master alloys are purchased commercially. The master alloy was cut into a cuboid with dimensions of $20 \times 8 \times 2$ mm^3 by a low-speed wire electrical discharge machining (WEDM-LS, AP250LS, Sodick, Japan). And the surface was subsequently polished with sandpaper for UVT experiments.

2.2. Ultrasonic vibration treatment (UVT) setup

The ultrasonic sonotrode generator generates an initial ultrasonic signal with a frequency of 20 kHz, and an ultrasonic sonotrode with a diameter of 5 mm was selected to obtain a high-frequency mechanical vibration through signal conversion. Firstly, a special fixture was used to fix the sample on the experimental bench, to maintain the stability of the sample under the energy of high frequency vibration. Secondly, we set processing parameters on the control panel and then started the ultrasonic vibration machine. With the downward movement of the ultrasonic sonotrode, high frequency ultrasonic vibration was applied. It should be noted that the impact was exerted on the near-surface zone. Finally, the sonotrode left a circular indentation on the surface of the sample. In order to obtain the desired experimental results, a series of parameters (amplitude, pressure and energy, etc.) were adjusted after several experiments, and finally-three sets of suitable experimental parameters were determined. Table S1 lists the experimental data parameters.

2.3. Structure characterization

The atomic structure was characterized in a JEM-2100F TEM with energy dispersive spectroscopy (EDS). HEA samples for TEM observation were prepared on a double beam system (FEI Scios). These samples were taken from the area of UVT. The microstructure in the deformation area of the samples was characterized by electron backscattered diffraction (EBSD). The samples were prepared by ion-beam polishing for 1 h at 6.5 kV. The EBSD characterizations were operated with a step size of $0.5 \sim 2$ μm at 20 kV.

2.4. Temperature and force measurement

To obtain the thermal effects of the process, an infrared thermographer with an accuracy of 1 °C was used to monitor temperature changes. The HEA sample was put on a dynamometer to receive the real-time force during ultrasonic vibration loading. The data-acquisition card (National Instruments NI-9237) was used to collect and process the force data with a frequency of 2,000 Hz.

2.5. Mechanical testing

In the compression experiment, the samples were made into a cylinder with a height of 1.8 mm and a diameter of 1.5 mm by using WEDM-LS for the ultrasonic vibration treated area. A universal material testing machine was used to perform multiple compression experiments on the samples. The compression properties of the micropillars were tested on a nanoindentation testing system (Hysitron TI950). The hardness of the samples was measured by a FMARS9000 automatic micro hardness instrument to do a mapping over a 2×2 mm^2 region, the hardness of the cross section of the UVT treated area was also tested.

3. Results

3.1. UVT experiment results

In the present work, UVT experiments were carried out in four groups of samples. The purpose was to transform the crystalline structure of HEA into an amorphous phase structure, as shown in Fig. 1a-c. Generally, the whole process would last only a few seconds. Taking 15000 J energy treated sample as an example, HEA samples before and after UVT are shown in Fig. 1d. The local deformation zone is exactly where the amorphous phase appears. From the force data collected in the experiments, the average stress is about 23 MPa (Fig. 1e). Obviously, this is a low stress experiment. Fig. 1f shows the thermogram at the highest temperature during the UVT process, and Fig. 1g shows the temperature curve of the UVT process. The temperature curve of the 15000 J sample shows that the maximum temperature rise throughout is less than 200 °C, which is far below its melting point of the equiatomic CoCrFeNiMn HEA. That is to say, the possibility of an amorphous phase formed by rapid cooling can be excluded.

3.2. Amorphous phase under TEM

To better investigate the formation process of the amorphous phase, the microscopic morphology, the corresponding selected area electron diffraction (SAED) patterns and the selected-area HRTEM images of the as-received, 5000 J, 10000 J and 15000 J samples are shown in Fig. 2. Fig. 2a-c illustrate that the as-received sample is a typical FCC structure. It can be clearly seen that the SAED of FCC matrix at [122] zone axis (Fig. 2b) and typical FCC matrix (Fig. 2c). Fig. 2d-f are the TEM images after 5000 J energy UVT, the selected section is no longer as complete as the FCC structure. Several diffraction rings and heterogeneous diffraction spots also indicate that the FCC structure of HEA has been difficult to observe by TEM. And it transforms from a single crystal structure to multiple fine crystals + internal amorphous structure. This structure is closer to the polycrystalline, which is similar to a typical polycrystalline diffraction ring (Fig. 2e). After further analysis, we can see the HRTEM image reveals that some amorphous phases

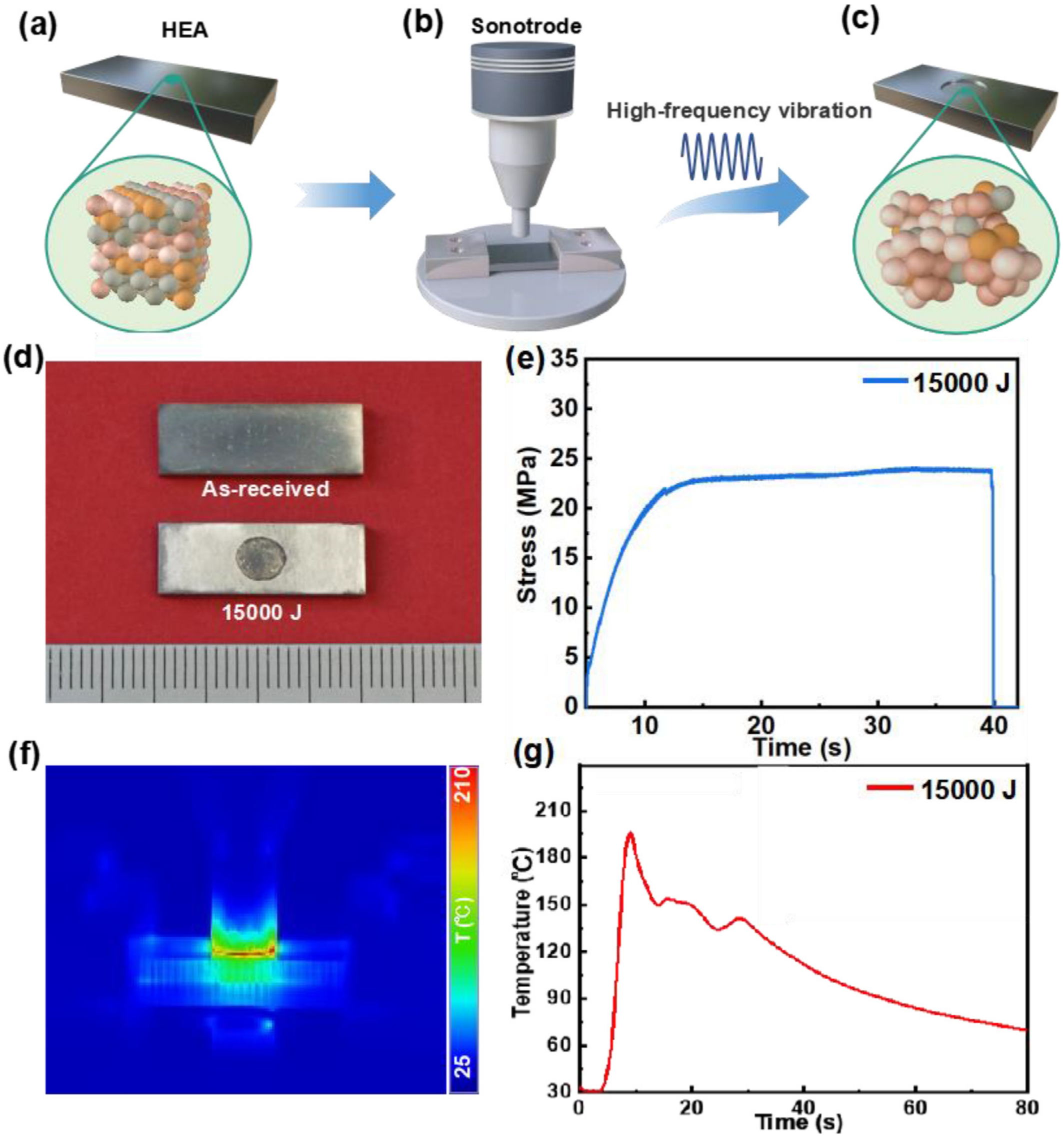

Fig. 1. Ultrasonic vibration treatment of HEA. (a) Schematic diagram of the sample and its internal atomic structure. (b) Schematic diagram of UVT device. (c) Schematic diagram of the treated sample and its internal atomic structure. (d) Comparison of 15000 J energy treated samples before and after UVT. (e) The stress-time curve of UVT process (15000 J). (f) Infrared thermographic image of the highest temperature point (15000 J). (g) Temperature profile of the UVT process (15000 J).

are interspersed among numerous small grains with different crystal orientations, as shown in Fig. 2f. The inset is the corresponding fast Fourier transform (FFT) pattern, which is similar to the result of the SAED image. This is the initial stage of amorphous phase formation. Immediately afterwards, we tried the UVT with 10,000 J and many slip bands and high density of dislocations appear, which can be seen in Fig. 2g. Amorphous diffuse halo rings and diffraction spots appear in Fig. 2h, indicating that there are both amorphous and crystalline phases here. The increase of the amorphous phase is clearly seen in Fig. 2i, and the amorphous phase is interspersed with many nanocrystals about 5 nm. Fig. 2j shows the morphology of the 15000 J sample observed under TEM. The corresponding SAED pattern of this region is shown in Fig. 2k. Surprisingly, when the input energy is increased to 15000 J, the amorphous phases are formed more uniformly and densely in Fig. 2l compared with Fig. 2i, although some nanocrystals are also present. Also, the amorphous diffuse halo ring is more obvious. In general, Fig. 2 shows the direct observational evidence of amorphous phase in the HEA crystal phase. However, the proportion of the amorphous phase to the overall crystalline phase remains low (Discussion and Supplementary Materials will further explain). The amorphous phase clearly visible under TEM laid the foundation for the subsequent work.

In more detail, we selected a sample treated with 15000 J energy and observed the characteristics of different regions by TEM. An amorphous-crystalline-amorphous TEM image was presented to demonstrate the transition between the two phases (Fig. 3a). Fig. 3b is the corresponding FFT pattern of Fig. 3a, showing the obvious amorphous ring and crystalline phase diffraction spots. In this case, three regions (R1, R2, *R*3) were chosen for specific observation. R1 is an amorphous region (Fig. 3c). The corresponding FFT pattern (Fig. 3f) has a clear amorphous ring. The R2 region is a typical crystal structure, which can be clearly seen from the results in Fig. 3d and Fig. 3g. The *R*3 region is an amorphous region, and the disordered structure can be clearly observed in the magnified Fig. 3e. Also its corresponding FFT pattern (Fig. 3h) can prove this. Another amorphous-crystalline transition structure is also shown in the supplemental material (Fig. S1). An EDS mapping is performed of the region in Fig. S1a. Element segregation and aggregation are not observed in the results (Fig. S1b-f). The distri-

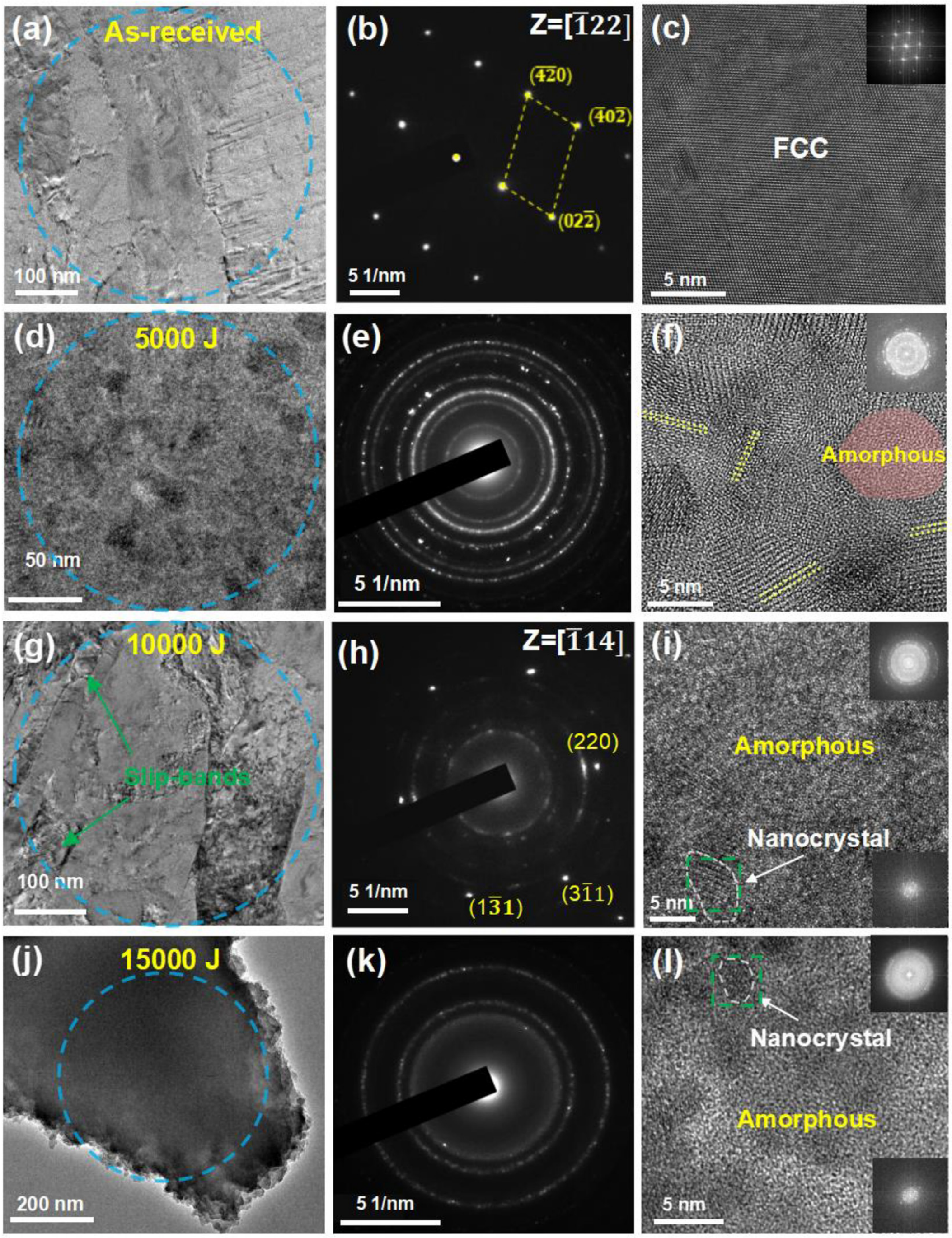

Fig. 2. The crystal-amorphous transition process of HEA treated by UVT. (a, d, g, j) The TEM morphologies of the untreated, 5000 J energy treated, 10000 J energy treated and 15000 J energy treated samples, respectively. The blue circle area is the corresponding SAED area. (b, e, h, k) The diffraction patterns correspond to (a), (d), (g) and (j). (c, f, i, l) The HRTEM images of the untreated, 5000 J energy-treated, 10000 J energy-treated and 15000 J energy-treated samples, respectively, and the insets are the FFT patterns. Where the FFT patterns in the lower right corner of (i) and (l) correspond to the green boxed region.

bution of various elements is uniform. Additional evidence of amorphous is provided in supplementary materials (Fig. S2).

Here we describe the volume fraction of the sample where the amorphous occurs, so we give the volume fraction of amorphization roughly by the process of FIB sampling and TEM characterization. First, the sampling depth of FIB is about 6 μm, and the effective observation area after ion thinning is about 5*5 μm (as shown in Fig. S3). We can find the amorphous phase in the whole sample by high-resolution TEM. After some statistics and analysis (please see Supplementary Material Fig. S4 for details), we determined that the area occupied by the amorphous phase is about 15 %. Therefore, we presume that the volume fraction of sample amorphization is 15 % and its depth is at least 5 μm.

3.3. Mechanical properties

At the macroscopic level, we characterized the mechanical properties of the samples to investigate how the UVT would bring to them. The compression experiments were performed on three treated samples as well as the original samples. After further mea-

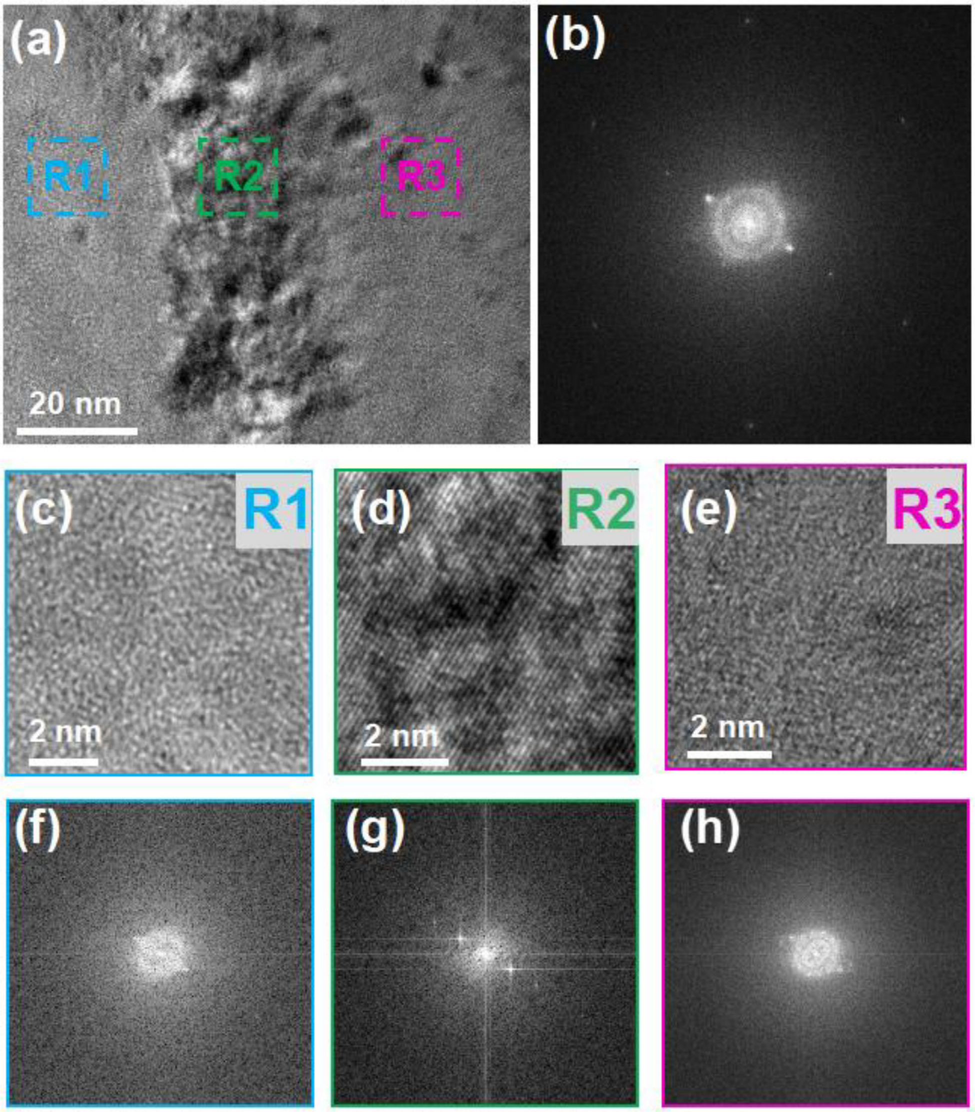

Fig. 3. Detailed analysis of 15000 J energy treatment sample. (a) TEM images of the amorphous-crystalline-amorphous transition structure. (c,d,e) are enlarged views of the R1-3 region in (a), respectively. (b,f,g,h) are the corresponding FFT patterns of (a,c,d,e), respectively.

surement, it was found that the height of all samples which h > 1.8 mm. So, to ensure the consistency of samples size, we made the height of the samples uniform at h = 1.80 ± 0.03 mm (Fig. S5). Fig. 4a shows the compression curves of the four samples. The yield strength was calculated as the stress value corresponding to 0.2 % residual deformation. The corresponding yield strength for each sample was obtained after multiple data sets were calculated. The strengths of the as-received sample, 5000 J sample, 10000 J sample and 15000 J sample are ~ 282 MPa, ~314 MPa, ~377 MPa and ~ 398 MPa, respectively. It can be seen that the yield strength of HEA increases with the increment of energy input. The maximum strength is increased by 41 %.

To explore the effect of UVT from the top to the bottom of the specimen, a cross-sectional hardness test of the UVT treated area was done. The results are shown in Fig. 4b and it was found that UVT only affected the hardness of the sample to a depth of approximately 0.6 mm and did not affect the hardness of the bottom of the sample. In addition, the hardness of the UVT-treated samples was measured by a microhardness tester to do a mapping over a 2×2 mm^2 region. The results of the surface mapping diagram for hardness are shown in Fig. 4c. The average hardness of the four samples are about 265 HV, 277 HV, 298 HV, and 328 HV, with a maximum hardness increase of about 24 %. Both the strength and hardness of the samples are positively and linearly correlated with the experimentally applied ultrasonic vibration energy.

In addition, UVT affects mainly the surface area, so we added a micropillar compression experiment. The experiment was performed using a pillar of 3 μm height and 3 μm diameter prepared by FIB (Fig. 5a), and the compression experiment was performed on a nano-indenter using a 10 μm diameter indenter. The result data obtained from the micropillar compression experiments are shown in Fig. 5b, and the strengths of the as-received, 5000 J, 10000 J and 15000 J samples are ~ 850 MPa, ~1000 MPa, ~1180 MPa and ~ 1300 MPa, respectively. At the microscopic level, the UVT samples still show the pattern that the higher the treatment energy, the higher the yield strength. 15000 J samples show a maximum strength increase of 53 %.

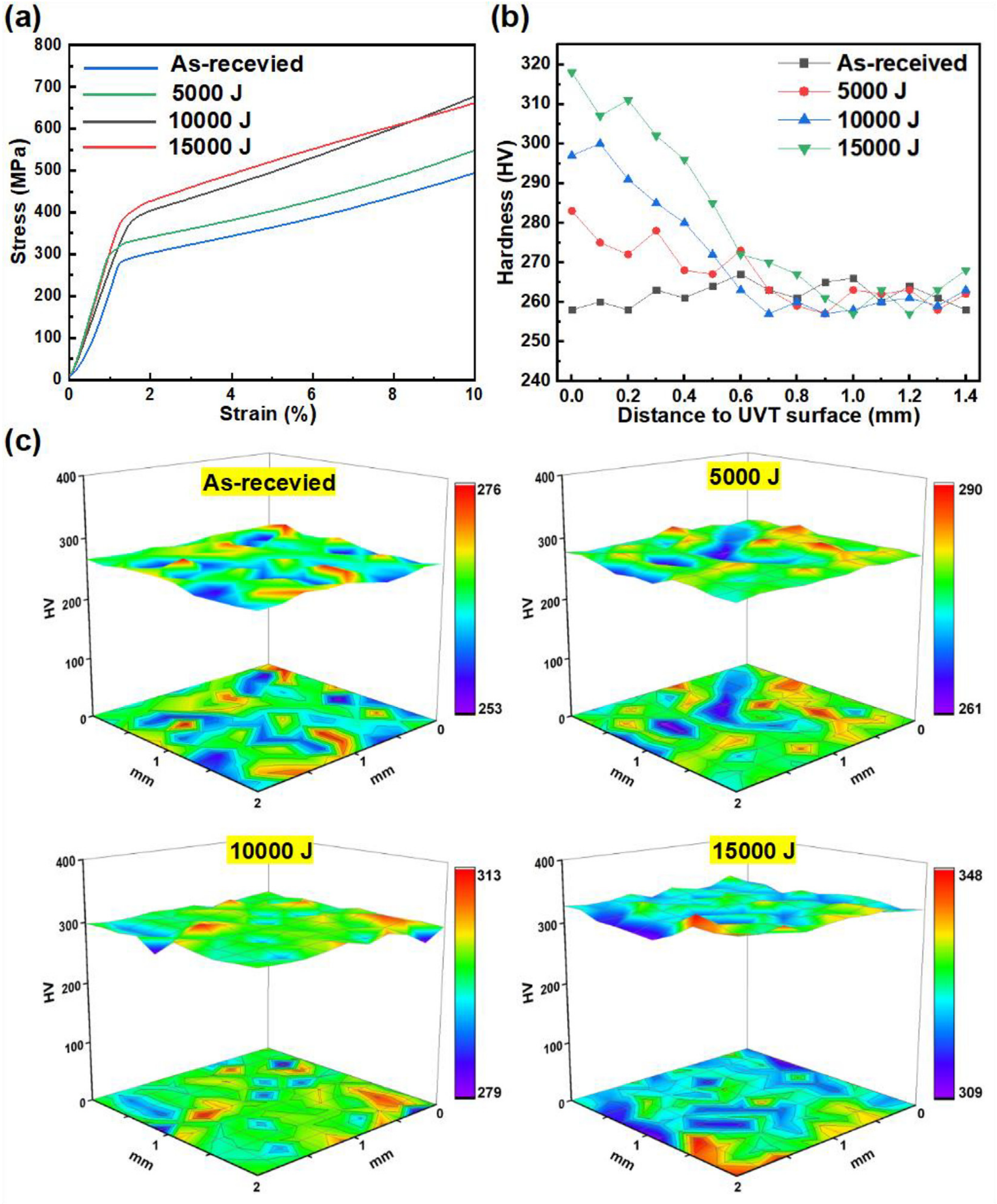

Fig. 4. Improvement of mechanical properties. (a) Compression curves for untreated sample, 5000 J energy-treated sample, 10000 J energy-treated sample, and 15000 J energy-treated sample. (b) Cross-sectional hardness for four types of samples. (c) Surface hardness mapping for four types of samples.

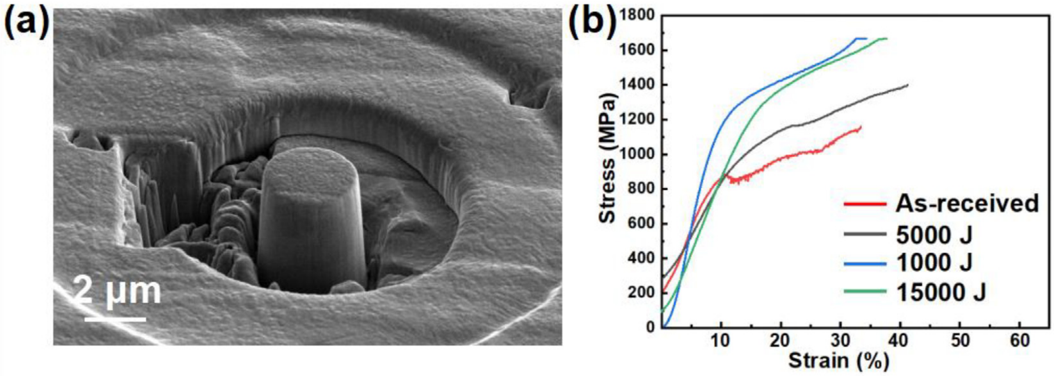

Fig. 5. (a) SEM image of micropillar. (b) Stress–strain curves of micropillar compression.

4. Discussion

4.1. Mechanism of the amorphization process

Although there is extensive research on the field of amorphization, the mechanisms of amorphization are still the subject of much research and discussion [30–32]. Thus, we need to further analyze the mechanism of UVT-induced amorphization in CoCrFeNiMn HEAs. The internal atomic structure was mainly observed by HRTEM to verify the transition from crystal to amorphous. Taking the 10,000 J energy-treated sample as an example (Fig. 6a), we observed a variety of structures by TEM and analyzed them in detail. In the area shown in Fig. 6a, amorphous and crystalline dominate most of the area, as shown in the supplementary materials (Supplementary Fig. S2d-f). A TEM-EDS line scan of this region was performed to amorphous region and FCC matrix (Supplementary Fig. S6). No obvious compositional differences between the amorphous regions and the FCC matrix were detected. To verify that the crystal-to-amorphous transition of this alloy is polymorphic solid-state amorphization (SSA), the chemically averaged compositions of the individual elements were measured in EDS line scan data across the amorphous-crystalline interface: Co-20 at%, Cr-17 at%, Fe-17 at%, Mn-23 at%, and Ni-25 at%. This suggests that the observed amorphous phases are not caused by chemical reactions occurring during the experiment, but may be due to deformation brought about by high-frequency ultrasonic vibrations. The SSA is commonly found in most crystalline materials [33,34], which is a phenomenon worthy of in-depth study.

A significant number of dislocations, twins and amorphous phases were found by TEM characterization (Fig. 6b) and high-

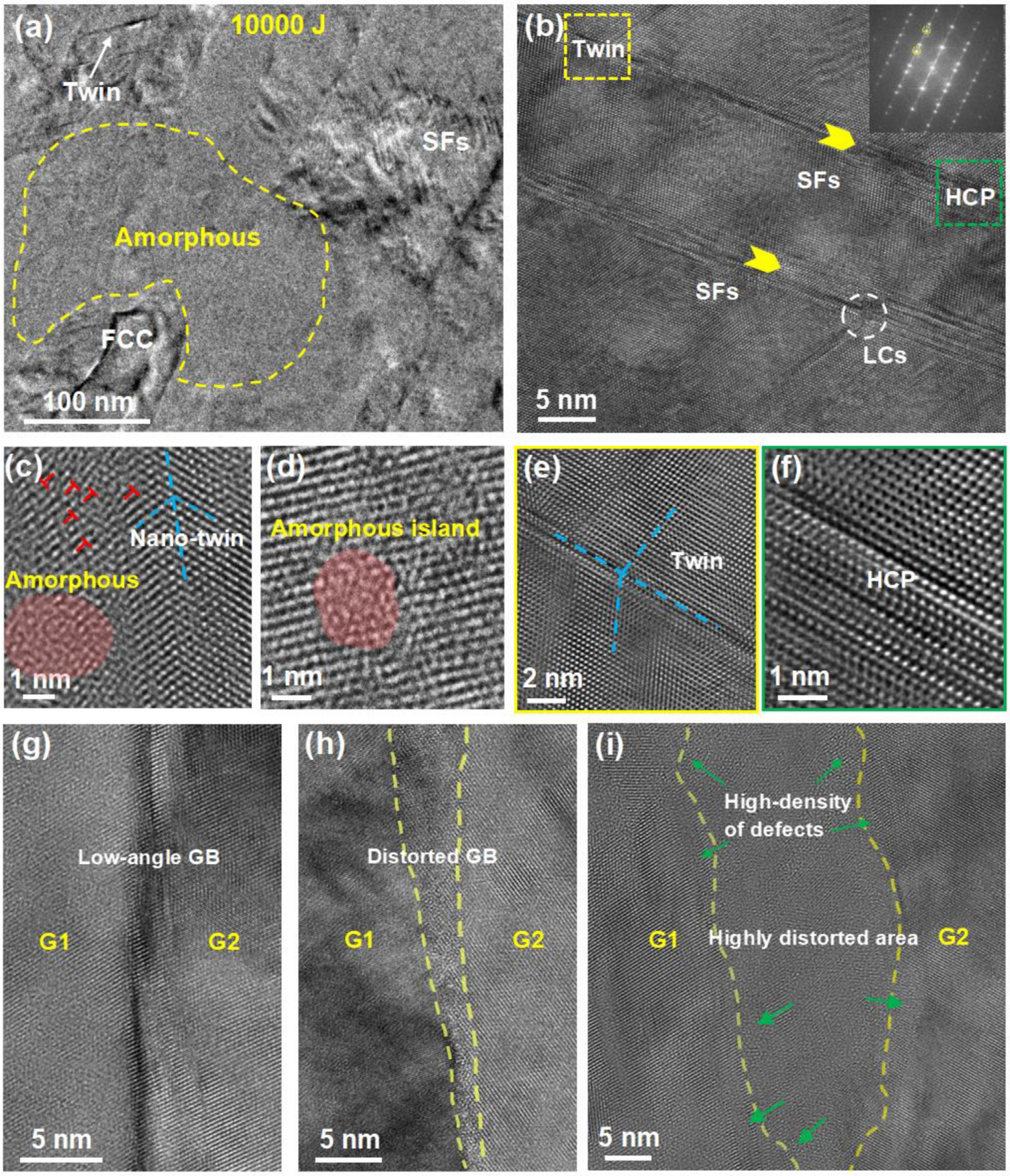

Fig. 6. Analysis of the amorphization. (a) Local morphology of the 10,000 J energy treatment sample. (b) TEM image of the SFs region selected from (a). The complex layer dislocation and twinning regions. (c) HRTEM image of the twin region selected from (a). Dislocations are marked with the symbol ⊥. (d) Selected HRTEM image of the FCC region from (a). Amorphous island in the FCC matrix is shown. (e) HRTEM image of the yellow region selected from (b). Demonstrates the details of the twin. (f) HRTEM image selected from the green region of (b). HCP structure of the atoms is shown. (g) TEM image of low-angle GB shows ordered states. (h) TEM image of high-angle GB, disordered state. (i) HRTEM image of the two grains at the GB. The green arrows are highlighted at the high-density defects.

lighted in Fig. 6c. It is worth mentioning that many amorphous islands with sizes around 2–3 nm were found in the FCC region (Fig. 6d), and similar areas we have observed in many places (shown in Fig. S7). Fig. 6b illustrates the SFs region with the corresponding FFT pattern inserted to show the formation of SFs. The yellow boxed area corresponds to the enlarged figure of Fig. 6e, showing the twin. The green boxed area corresponds to Fig. 6f, where the SFs region is most likely to show the FCC → HCP phase transition. Because the current equiatomic HEA has a low SF energy [35]. Zaddach et al. [36] used density functional theory to calculate SF energy and obtained that the value of CrMnFeCoNi HEA at 0 K was only 20 mJ/m^2. The presence of HCP, on the other hand, induces the transition from the crystalline phase to the amorphous phase more easily. Crossed SFs in Fig. 6b form Lomer-Cot-trell locks (LCs), and the lower SF energy promotes the formation of LCs, twins and HCP bands. Of more interest to us is another scenario where amorphization occurs in the grain boundaries (GBs). For now, abundant literature has reported examples of crystal GB amorphization [37–42], which is a reliable explanatory path for crystal amorphization. Simulations in the literature show that internal boundaries tend to be the preferred nucleation sites for migrating dislocations, resulting in dislocation obstruction and dislocation pile-ups [43,44]. Fig. 6g shows the junction of two grains G1 and G2 with a low-angle GB, which is in an ordered state. Fig. 6h shows the junction of two grains whose GBs are high-angle GBs, which is identified as disordered in the literature [37]. High-frequency vibrations can easily squeeze or stretch the atoms between GBs, and Fig. S8 gives a sketch for high-angle GBs to explain this phenomenon. This means that high-angle GBs are the most likely locations for amorphous phases. In Fig. 6h, it is clear that the disorder region at the grain boundaries expands from bottom to top. In Fig. 6i, the disorder region expands again at any time with the continuous input of ultrasonic energy. The precursors of amorphous phase are gradually formed at the GB, and there are severe lattice distortions. Heavily distorted regions are sandwiched between the grains, these regions are in the metastable mesophase and are most susceptible to transformation to the amorphous phase under continuous ultrasonic vibration. Close to the grain surroundings are some high-density defects (green arrows), which are also precursors to amorphization. There are similar reports in the relevant literature [45]. Thus, from Fig. 6g-i, we believe that the main mechanism dominating amorphization of HEA in UVT is GB amorphization.

Grain refinement, which is considered to be the first step before the onset of amorphization [46]. In ball milling amorphization, only crystals with grain size less than 100 A undergo amorphous transformation during the ball milling process [47]. The grain refinement process is not difficult to see in the TEM images (Fig. 2c → 2f), with a large number of nanocrystals present in Fig. 2f, and the wider diffraction pattern in this region also shows a typical polycrystalline diffraction ring (Fig. 2e). Supplementary material Fig. S9 gives an EBSD pattern of the as-received sample, illustrating that the grains of the commercially purchased samples are super-sized. After UVT, the super-sized grains break up and a large number of nanocrystals appear. The black and white patches shown in Fig. S10 in the supplementary material are the nanocrystals. After a certain degree of grain refinement, the nanocrystal structure is unstable and ideal for promoting SSA [48,49]. In addition, after grain refinement, the percentage of sub-GBs increases significantly and the degree of confusion is elevated, which in this case is highly conducive to the spread of amorphous phases. From the kinetic perspective, high-frequency sustained ultrasonic vibrations can provide enough momentum for atoms in disordered GBs to move to a metastable position. When metastable atoms are prevalent, then providing energy as a driving force to drive the atoms can easily lead to amorphization [50,51]. From thermodynamic perspective, increasing the number of GBs by reducing the grain size introduces disordered structures, thereby increasing the energy storage of the system. Meanwhile, UVT can provide energy to the sample. In summary, grain refinement, as a necessary prerequisite for amorphization, is a crucial part of this work.

In the grain interior, SSA is generally an amorphization that occurs at high strain and/or high strain rate. At high strain rates, there is not enough time for the sample to activate the plastic deformation mode [52]. In our work, UVT produced a local deformation of the sample, forming a pit of 2–3 mm in the middle. But the deformation process is very rapid, and UVT meets this characteristic of high strain rate. When the partial crystalline transformation to amorphous is completed in a very short period of time, it will skip the phase transformation modes of twinning, layer dislocation, and FCC → HCP. It is worth noting that the ultrasonic vibration not only collapses the sample surface area once, but repeatedly and rapidly impacts the sample surface numerous times. This process is actually adding defects to the samples continuously. Under ultrasonic vibrations at high frequencies, it is extremely easy to cause mechanical instability of the crystalline phase [53]. In this case, defects (e.g., dislocations and point defects) tend to appear inside the grains. Once the defects accumulate to a certain concentration, they converge to form nano-amorphous islands. With the input of ultrasonic vibration energy, the amorphous islands increase and interconnect. It is likely to form a large region of amorphous phase within the crystal. The appearance of amorphous islands within the crystal (secondary mechanism), can be used as a complement to the amorphization at the grain boundaries (primary mechanism).

We can envision an abbreviated process of amorphization represented by the schematic diagram shown in Fig. 7. The TEM pictures in Fig. 7a correspond to the schematic process in Fig. 7b. In Fig. 7b, UVT causes the grain refinement of the equiatomic CoCrFeNiMn HEA to occur first, when disorder boundaries start to appear. Subsequently, high-frequency ultrasonic vibration continues to provide deformation energy, and the volume fraction share of disordered boundaries increases significantly. In other words, the disordered regions (yellow lines in Fig. 7b) expand, cross, and nucleate at the GB with the increase of dislocation density to eventually form a large amorphous phase. If the defect density is the variable, then the disordered phase generation starts with point defects and dislocations (Fig. 7c). As the defect density increases, twins appear. And then, the increase in defect density and the proliferation of SFs make it easy for phase transformation to occur. Eventually, the highest strain state of amorphization is reached. Generally, SSA follows basically this process. However, since the amorphization process is complex and diverse, there are cases where the intermediate stages can be directly skipped, such as the amorphous islands that appear in this work. Our results presented above may provide new insights to understand the nature of the crystal to amorphous transition.

4.2. Mechanical properties of HEAs after UVT

On the macroscopic compression experiments, it can be concluded that UVT treatment has an enhancement effect on the strength. In the 5000 J sample, the apparent increase in strength is mainly due to grain refinement (less amorphous phase at this point). In the case of the 10,000 J and 15,000 J samples, the amorphous phase plays a very important role. Because there is a limit to the refinement of the grain, it cannot be refined indefinitely. So, the contribution of amorphous phase in mechanical properties - as a barrier to dislocation propagation [54–55]. And the amorphous phase should be harder than its crystalline counterpart, crystalline-amorphous nanolaminates enhance the strength and hardness of the material [56–57]. In addition, the grain refinement

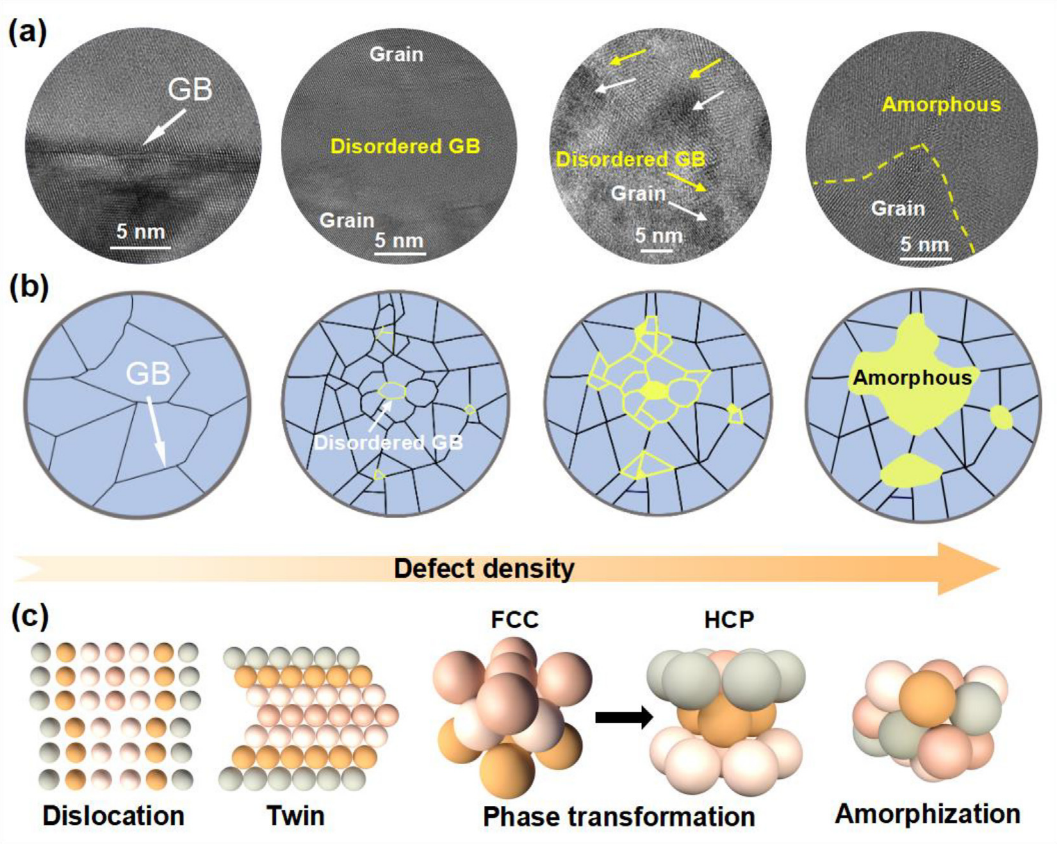

Fig. 7. Proposed hierarchical deformation mechanism paradigm for equiatomic CoCrFeNiMn HEAs. (a) HRTEM images of HEA samples. In the process of grain refinement after UVT, the amorphous phases are produced as the crystal grains are refined. (b) The yellow lines in the four models represent the disordered regions of grain boundaries. With the increase of dislocation density, the final SSA occurs. (c) Highlight the details of the mechanism of amorphous, showing dislocations, twinning, phase transitions and amorphous phases. In general, triggering the next mechanism requires the creation of additional defects (energy source). The model is a holistic orientation in which the various mechanisms are interacting to form intricate microstructures.

and the increase of dislocation density have enhanced effects on the strength and hardness of the material. Therefore, the UVT-treated high-entropy alloys has these special microstructures, which are able to enhance the strength and hardness substantially.

In microscopic samples, micropillar compression similarly demonstrated the ability of UVT to enhance the strength of HEA. In terms of yield strength, the microscopic samples were approximately 3x higher than the macroscopic samples. This happens due to the extrinsic size effect of small samples. This size effect is determined by the size of the dislocation source [58]. At least we can be sure that the as-received sample is due to this reason, because its grains are not refined. While the 5000–15000 J samples are more complex internally, we cannot exclude that they do not receive size effects. And, they may still be in the presence of internal stresses, which would likewise lead to an increase in strength. But in macroscopic compression, the depth of UVT influence is at 1/3 of the surface, and overall, the internal stress will have much less effect on the strength. In addition, we did not consider the effect of strain rate on strength when doing micropillar compression experiments. In the micropillar compression experiments, the higher the strain rate the greater the strength enhancement [59]. Therefore, it will be more interesting to design more systematic and rational experiments to explore the microscopic properties of UVT in future work.

5. Conclusion

All in all, we propose a rapid and facile amorphization UVT method for the multi-component HEA under low stress and temperature. We are able to roughly estimate an amorphization volume fraction of 15 % at a depth of 5 μm on the sample surface. The equiatomic FCC structure of CoCrFeNiMn HEA can generate a variety of microstructural morphologies by UVT in seconds, including nanocrystalline, SFs bands, twins, HCP lamellae, amorphous bands, and amorphous islands. GB amorphization plays a dominant role in the amorphization process of HEA. Grain refinement and the introduction of amorphous phases improve the mechanical properties of this material. At the macroscopic level, the yield strength is increased by 41 % and the hardness is increased by 24 %. On the microscopic level, the yield strength was increased by 53 %. Our results throw lights on the revealing of the order–disorder transition in alloys and provide new ways to realize the strengthening of metallic materials.

CRediT authorship contribution statement

Caitao Fan: Methodology, Investigation, Visualization, Writing – original draft, Writing – review & editing. **Luyao Li:** Methodology. **Wenxin Wen:** Investigation. **Hongzhen Li:** Investigation. **Jianan Fu:** . **Wenqing Ruan:** Supervision. **Shuai Ren:** Supervision. **Sajad Sohrabi:** Supervision. **Zhenxuan Zhang:** Supervision. **Xiong Liang:** Conceptualization, Writing – review & editing. **Jiang Ma:** Conceptualization, Writing – review & editing.

Data availability

No data was used for the research described in the article.

Declaration of Competing Interest

The authors declare that they have no known competing financial interests or personal relationships that could have appeared to influence the work reported in this paper.

Acknowledgements

The authors thank the assistance on microscope observation received from the Electron Microscope Center of the Shenzhen University.

Funding

The work was supported by the Key Basic and Applied Research Program of Guangdong Province, China (Grant Nr. 2019B030302010), the National Natural Science Foundation of China (Grant Nr. 52122105, 52271150, 51971150 and 52201185), the National Key Research and Development Program of China (Grant No. 2018YFA0703604), the Guangdong Basic and Applied Basic Research Foundation (Grant Nr. 2020B1515120092).

Data and material availability

All data needed to evaluate the conclusions in the paper are present in the paper and/or the supplementary materials.

Appendix A. Supplementary material

Supplementary data to this article can be found online at https://doi.org/10.1016/j.matdes.2022.111575.

References

[1] J.W. Yeh, S.K. Chen, S.J. Lin, J.Y. Gan, T.S. Chin, T.T. Shun, C.H. Tsau, S.Y. Chang, Nanostructured high-entropy alloys with multiple principal elements: novel alloy design concepts and outcomes, Adv. Eng. Mater. 6 (5) (2004) 299–303.

[2] M.J. Yao, K.G. Pradeep, C.C. Tasan, D. Raabe, A novel, single phase, non-equiatomic FeMnNiCoCr high-entropy alloy with exceptional phase stability and tensile ductility, Scr. Mater. 72–73 (2014) 5–8.

[3] B. Cantor, I.T.H. Chang, P. Knight, A.J.B. Vincent, Microstructural development in equiatomic multicomponent alloys, Mater. Sci. Eng. A 375–377 (2004) 213–218.

[4] D.B. Miracle, O.N. Senkov, A critical review of high entropy alloys and related concepts, Acta Mater. 122 (2017) 448–511.

[5] H. Shahmir, T. Mousavi, J. He, Z. Lu, M. Kawasaki, T.G. Langdon, Microstructure and properties of a CoCrFeNiMn high-entropy alloy processed by equal-channel angular pressing, Mater. Sci. Eng. A 705 (2017) 411–419.

[6] F. Otto, Y. Yang, H. Bei, E.P. George, Relative effects of enthalpy and entropy on the phase stability of equiatomic high-entropy alloys, Acta Mater. 61 (7) (2013) 2628–2638.

[7] N. Stepanov, M. Tikhonovsky, N. Yurchenko, D. Zyabkin, M. Klimova, S. Zherebtsov, A. Efimov, G. Salishchev, Effect of cryo-deformation on structure and properties of CoCrFeNiMn high-entropy alloy, Intermetallics 59 (2015) 8–17.

[8] B. Gludovatz, A. Hohenwarter, D. Catoor, E.H. Chang, E.P. George, R.O. Ritchie, A fracture-resistant high-entropy alloy for cryogenic applications, Science 345 (6201) (2014) 1153.

[9] Z.P. Lu, H. Wang, M.W. Chen, I. Baker, J.W. Yeh, C.T. Liu, T.G. Nieh, An assessment on the future development of high-entropy alloys: summary from a recent workshop, Intermetallics 66 (2015) 67–76.

[10] Y.F. Ye, Q. Wang, J. Lu, C.T. Liu, Y. Yang, High-entropy alloy: challenges and prospects, Mater. Today 19 (6) (2016) 349–362.

[11] M.H. Tsai, J.W. Yeh, High-entropy alloys: a critical review, Mater. Res. Lett. 2 (3) (2014) 107–123.

[12] H. Wang, D. Chen, X. An, Y. Zhang, X. Liao, Deformation-induced crystalline-to-amorphous phase transformation in a CrMnFeCoNi high-entropy alloy, Sci. Adv. 7 (14) (2021) eabe3105.

[13] S. Zhao, Z. Li, C. Zhu, W. Yang, M.A. Meyers, Amorphization in extreme deformation of the CrMnFeCoNi high-entropy alloy, Sci. Adv. 7 (5) (2021) 3108–3137.

[14] K. Ming, W. Lu, Z. Li, X. Bi, J. Wang, Amorphous bands induced by low temperature tension in a non-equiatomic CrMnFeCoNi alloy, Acta Mater. 188 (2020) 354–365.

[15] W. Wu, S. Ni, Y. Liu, B. Liu, M. Song, Amorphization at twin-twin intersected region in FeCoCrNi high-entropy alloy subjected to high-pressure torsion, Mater. Charact. 127 (2017) 111–115.

[16] Y.-L. Chen, C.-W. Tsai, C.-C. Juan, M.-H. Chuang, J.-W. Yeh, T.-S. Chin, S.-K. Chen, Amorphization of equimolar alloys with HCP elements during mechanical alloying, J. Alloys. Compd. 506 (1) (2010) 210–215.

[17] M. Vaidya, S. Armugam, S. Kashyap, B.S. Murty, Amorphization in equiatomic high entropy alloys, J. Non. Cryst. Solids 413 (2015) 8–14.

[18] Z.H. Cao, Y.J. Ma, Y.P. Cai, G.J. Wang, X.K. Meng, High strength dual-phase high entropy alloys with a tunable nanolayer thickness, Scr. Mater. 173 (2019) 149–153.

[19] S. Fang, C. Wang, C.-L. Li, J.-H. Luan, Z.-B. Jiao, C.-T. Liu, C.-H. Hsueh, Microstructures and mechanical properties of CoCrFeMnNiV high entropy alloy films, J. Alloys. Compd. 820 (2020) 153388.

[20] B. Li, L. Zhang, B. Yang, Grain refinement and localized amorphization of additively manufactured high-entropy alloy matrix composites reinforced by nano ceramic particles via selective-laser-melting/remelting, Compos. Commun. 19 (2020) 56–60.

[21] J. Li, W. Craeghs, C. Jing, S. Gong, F. Shan, Microstructure and physical performance of laser-induction nanocrystals modified high-entropy alloy composites on titanium alloy, Mater. Des. 117 (2017) 363–370.

[22] J. Ma, C. Yang, X. Liu, B. Shang, Y. Yang, Fast surface dynamics enabled cold joining of metallic glasses, Sci. Adv. 5 (11) (2019) eaax7256.

[23] Z. Li, S. Yuan, J. Ma, J. Shen, A. Batako, Study on the surface formation mechanism in scratching test with different ultrasonic vibration forms, J. Mater. Process. Technol. 294 (2014) (2021) 117108.

[24] X. Liang, C. Fan, J. Fu, Z. Liu, Z. Zhang, S. Ren, W. Ruan, H. Shi, Improve the forming ability of Al-Based metallic glass under ultrasonic vibration at room temperature, Front. Mater. 8 (2021) 746955.

[25] X. Li, D. Wei, J.Y. Zhang, X.D. Liu, Z. Li, T.Y. Wang, Q.F. He, Y.J. Wang, J. Ma, W.H. Wang, Y. Yang, Ultrasonic plasticity of metallic glass near room temperature, Appl. Mater. Today 21 (2020) 100866.

[26] Z. Huang, J. Fu, X. Li, W. Wen, H. Lin, Y. Lou, F. Luo, Z. Zhang, X. Liang, J. Ma, Ultrasonic-assisted rapid cold welding of bulk metallic glasses, Sci. China Mater. 65 (2022) 255–262.

[27] Z. Lv, Y. Yan, C. Yuan, B. Huang, C. Yang, J. Ma, J. Wang, L. Huo, Z. Cui, X. Wang, W. Wang, B. Shen, Making Fe-Si-B amorphous powders as an effective catalyst for dye degradation by high-energy ultrasonic vibration, Mater. Des. 194 (2020) 108876.

[28] Y. Xiao, F. Sun, J.-Q. Ran, B. Wang, J.-M. Zhong, J. Ma, F. Luo, Ultrasonic micro punching with flexible punch for thin stainless sheet metal, Int. J. Adv. Manuf. Tech. 108 (9–10) (2020) 2763–2773.

[29] X. Liang, Y. Liu, Z. Liu, J. Ma, Z. Zhang, W. Ruan, S. Ren, T. Peng, X. Wu, H. Shi, Ultrasonic injection molding of glass fiber reinforced polypropylene parts using tungsten carbide-cobalt mold core, Mater. Des. 205 (2021) 109771.

[30] L. William, Johnson, Thermodynamic and kinetic aspects of the crystal to glass transformation in metallic materials, Prog. Mater. Sci. 81–134 (1986).

[31] H.J. Fecht, G. Han, Z. Fu, W.L. Johnson, Metastable phase formation in the Zr-Al binary system induced by mechanical alloying, J. Appl. Phys. 67 (4) (1990) 1744–1748.

[32] A.W, Weeber, H, Bakker, Amorphization by ball milling. A review, Phys. B: Phys. Condens. Matter. 153 1-3 1988 93-135.

[33] K. Xu, X. Xiong, Y. Zhai, L. Wang, S. Li, J. Yan, D. Wu, X. Ma, H. Li, Effect of milling conditions on solid-state amorphization of glipizide, and characterization and stability of solid forms, J. Pharm. Biomed. Anal. 129 (2016) 367–377.

[34] V. Caron, J.F. Willart, R. Lefort, P. Derollez, F. Danede, M. Descamps, Solid state amorphization kinetic of alpha lactose upon mechanical milling, Carbohydr. Res. 346 (16) (2011) 2622–2628.

[35] T.M. Smith, M.S. Hooshmand, B.D. Esser, F. Otto, D.W. McComb, E.P. George, M. Ghazisaeidi, M.J. Mills, Atomic-scale characterization and modeling of 60° dislocations in a high-entropy alloy, Acta Mater. 110 (2016) 352–363.

[36] A.J. Zaddach, C. Niu, C.C. Koch, D.L. Irving, Mechanical Properties and Stacking Fault Energies of NiFeCrCoMn High-Entropy Alloy, JOM 65 (12) (2013) 1780–1789.

[37] A. Oudriss, J. Creus, J. Bouhattate, E. Conforto, C. Berziou, C. Savall, X. Feaugas, Grain size and grain-boundary effects on diffusion and trapping of hydrogen in pure nickel, Acta Mater. 60 (19) (2012) 6814–6828.

[38] V. Samae, P. Cordier, S. Demouchy, C. Bollinger, J. Gasc, S. Koizumi, A. Mussi, D. Schryvers, H. Idrissi, Stress-induced amorphization triggers deformation in the lithospheric mantle, Nature 591 (7848) (2021) 82–86.

[39] M.Y, Gutkin, I.A, Ovid'ko, Transformations of low-angle tilt boundaries inhigh−Tcsuperconductors, Phys. Rev. B 63 6 2001 064515.

[40] G. Gutiérrez, M. Kiwi, R. Ramírez, Amorphization in the vicinity of a grain boundary: a molecular-dynamics approach, Phys. Rev. B: Condens. Matter. 54 (16) (1996) 11701–11705.

[41] R. Benedictus, K. Han, C. TræHolt, A. BoTtger, E.J. Mittemeijer, Solid state amorphization in Ni–Ti systems: the effect of structure on the kinetics of interface and grain-boundary amorphization, Acta Mater. 46 (15) (1998) 5491–5508.

[42] P. Keblinski, S.R. Phillpot, D. Wolf, H. Gleiter, Thermodynamic criterion for the stability of amorphous intergranular films in covalent materials, Phys. Rev. Lett. 77 (14) (1996) 2965.
[43] F. Bormann, R.H.J. Peerlings, M.G.D. Geers, B. Svendsen, A computational approach towards modelling dislocation transmission across phase boundary, Philos. Mag. 99 (17) (2019) 2126–2151.
[44] N. Jia, D. Raabe, X. Zhao, Crystal plasticity modeling of size effects in rolled multilayered Cu-Nb composites, Acta Mater. 111 (2016) 116–128.
[45] S. Zhao, E.N. Hahn, B. Kad, et al., Amorphization and nanocrystallization of silicon under shock compression, Acta Mater. 103 (2016) 519–533.
[46] A. Sagel, N. Wanderka, R.K. Wunderlich, P. Schubert-Bischoff, H.-J. Fecht, Early stages of solid-state amorphization reaction during mechanical alloying of a multicomponent Zr-Powder Mixture, Scr. Mater. 38 (1) (1997) 169.
[47] A. Calka, A.P. Pogany, R.A. Shanks, H. Engelman, Re-amorphization of crystallized metallic glass Co70.3Fe4.7Si15B10 ribbons by mechanical alloying, Mater. Sci. Eng. A 128 (1) (1990) 107–112.
[48] S. Han, L. Zhao, Q. Jiang, J. Lian, Deformation-induced localized solid-state amorphization in nanocrystalline nickel, Sci. Rep. 2 (2012) 493.
[49] G.P. Zheng, M. Li, Crystal instability in nanocrystalline materials, Acta Mater. 55 (16) (2007) 5464–5472.
[50] H.J. Fecht, P.J. Desré, W.L. Johnson, Thermodynamic aspects of solid-state amorphization: polymorphous melting Clapeyron diagram, Philos. Mag. B 59 (1989) 577–585.
[51] D. Wolf, P.R. Okamoto, S. Yip, J.F. Lutsko, M. Kluge, Thermodynamic parallels between solid-state amorphization and melting, J.mater.res 5 (02) (1990) 286–301.
[52] E. Ma, Amorphization in mechanically driven material systems, Scr. Mater. 49 (10) (2003) 941–946.
[53] M. Li, W.L. Johnson, Instability of metastable solid solutions and the crystal to glass transition, Phys. Rev. Lett. 70 (8) (1993) 1120.
[54] Z. Fan, S. Xue, J. Wang, K.Y. Yu, H. Wang, X. Zhang, Unusual size dependent strengthening mechanisms of Cu/amorphous CuNb multilayers, Acta Mater. 120 (2016) 327–336.
[55] B. Cheng, J.R. Trelewicz, Design of Crystalline-Amorphous Nanolaminates Using Deformation Mechanism Maps, Acta Mater. 153 (2018) 314–326.
[56] Y, Wang, J, Li, A V, Hamza Barbee T. Ductile crystalline-amorphous nanolaminates. Proceedings of the National Academy of Sciences, 104 27 2007 11155-11160.
[57] W. Gou, E.A. Jgle, P.P. Choi, J. Yao, A. Kostka, J. Schneider, D. Raabe, Shear-induced mixing governs codeformation of crystalline-amorphous nanolaminates, Phys. Rev. Lett. 113 (3) (2014) 035501.
[58] A, Triplicane, Parthasarathy, Satish I. Rao, Dennis M. Dimiduk, Michael D. Uchic and Dallas R. Trinkle. Contribution to size effect of yield strength from the stochastics of dislocation source lengths in finite samples. Scripta Materialia, 2007 56 313-316.
[59] L. Zhao, Q. Guo, Z. Li, Z. Li, G. Fan, D. Xiong, Y. Su, J. Zhang, Z. Tan, D. Zhang, Strain-rate dependent deformation mechanism of graphene-al nanolaminated composites studied using micro-pillar compression, Int. J. Plast 105 (2018) 128–140.